Biomacromolecules

Article

Cite This: Biomacromolecules 2019, 20, 1068−1076

pubs.acs.org/Biomac

Cancer Selective Turn-On Fluorescence Imaging Using a Biopolymeric Nanocarrier

Yoon Jeong,[†] Garam Kim,[‡,§] Soohyun Jeong,[†] Byungchul Lee,[§,∥] Sangeun Kim,[‡,§,∥] Won-Gun Koh,*[,⊥] and Kangwon Lee*[,†,∥]

[†]Program in Nanoscience and Technology, Graduate School of Convergence Science and Technology, Seoul National University, Seoul, 08826 Republic of Korea

[‡]Program in Biomedical Radiation Sciences, Graduate School of Convergence Science and Technology, Seoul National University, Seoul, 08826 Republic of Korea

[§]Department of Nuclear Medicine, College of Medicine, Seoul National University Bundang Hospital, Bundang, 13620 Republic of Korea

[∥]Advanced Institutes of Convergence Technology, Suwon, 16229 Republic of Korea

[⊥]Department of Chemical and Biomolecular Engineering, Yonsei University, Seoul, 03722 Republic of Korea

Supporting Information

ABSTRACT: Most nanoparticle-based bioresearch for clinical applications is unable to overcome the clinical barriers of efficacy (e.g., sensitivity and selectivity), safety for human use, and scalability for mass-production processes. Here, we proposed a promising concept of using a biocompatible nanocarrier that delivers natural fluorescent precursors into cancerous cells. The nanocarrier is a biopolymeric nanoparticle that can be easily loaded with fluorescent precursors to form a fluorescent moiety via a biosynthesis pathway. Once delivered into cancerous cells, the nanocarriers are selectively turned on and distinctively fluoresce upon excitation. We, therefore, demonstrated the efficacy of the selective turn-on fluorescence of the nanocarriers in in vitro coculture models and in vivo tumor-bearing models.

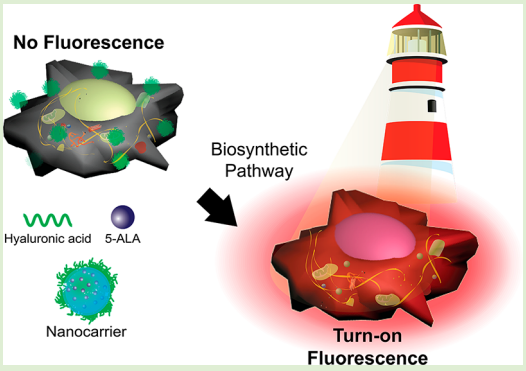

INTRODUCTION

Nanoparticle-based bioimaging technologies have received wide attention in biomedical fields for several decades.[1−6] The innovative development of novel nanoparticles conjugated with fluorophores has played a key role in the field of nanomedicine.[7−10] However, inevitable issues relating to safety are always a hindrance in their potential use. Moreover, good manufacturing practices that include the scale-up of manufacturing processes and compliance with Food and Drug Administration guidelines need to be critically considered from a commercialization perspective.[11,12] Therefore, most nanoparticle-based bioresearch remains at the preclinical status because it is unable to overcome clinical barriers with the exception of an extremely small number of studies in nanomaterials.[13,14] Hence, a novel approach is required for the clinical and practical medical use of fluorescent diagnosis.

To achieve a selective turn-on fluorescence in cancer cells,[15,16] many research groups have demonstrated the use of 5-aminolevulinic acid (5-ALA). This molecule is a natural, nonfluorescent, and metabolic precursor of protoporphyrin IX (PpIX).[17] However, despite several efforts in developing nanoparticles conjugated with or loaded with 5-ALA as a diagnostic agent for cancer cells,[18−24] fundamental problems such as low stability, short-term storage, and complex and expensive fabrication steps have not been addressed. Thus, these studies may also end up remaining at the in vitro stage.

Here, we introduce a promising approach of selective cancer diagnosis using natural materials to solve this issue. To our knowledge, no studies to date have succeeded in producing a nanosized carrier for the enhanced delivery of 5-ALA that allow for long-term storage.[25] Our approach to fabricate a highly stable nanocarrier is very simple to mass-produce, thus enabling cost reduction. Importantly, we used no chemical modification to circumvent additional toxic problems and/or complex manufacturing processes. Furthermore, we demonstrate other technical approaches to in vitro coculture models and in vivo local delivery methods to evaluate the efficacy of our nanocarriers. Our approach represents a cornerstone in the development of imaging agents for cancer cells.

EXPERIMENTAL SECTION

Preparation of Nanocarriers Encapsulating 5-ALA. Refined soybean oil, 5-ALA, sorbitan monoesters (Span 80), and polyethylene

Received: November 24, 2018
Revised: January 5, 2019
Published: January 15, 2019

DOI: 10.1021/acs.biomac.8b01690
Biomacromolecules 2019, 20, 1068−1076

glycol 20 (PEG-20) sorbitan monooleate (Tween 80) technical grade—suitable for cell culture—were purchased from Sigma. Hyaluronic acid (research grade) was purchased from Lifecore (MW = 91−175 kDa). By adjusting the Span to Tween ratio, various hydrophilic−lipophilic balance (HLB) values can be obtained, allowing the emulsification of many industrial raw materials. The mixed HLB value of cosurfactants was derived by multiplying the HLB values of Span 80 and Tween 80 with their weight fractions. The oily phase (soybean oil) contained cosurfactants (mixtures of Span 80 and Tween 80) and the aqueous phase (sodium hyaluronate, alginate acid, and 5-ALA), which were prepared separately in glass vials. The nanocarrier was prepared using soybean oil, cosurfactants, and an aqueous phase in a weight ratio of 7:1:2. The entire solution including soybean oil, cosurfactants, and the aqueous phase (1 wt % hyaluronic acid, 0.1 wt % alginate acid, and 1, 3, 5 wt % 5-ALA) was mixed thoroughly in a glass vial using a vortexer for 30 s. The solution mixture was ultrasonicated using a 6 mm probe tip-sonicator at an amplitude of 40% (Sonics, VC-750) for 10 min without any on−off pulse cycles. After ultrasonication, the bluish color of the mixture became transparent (or translucent). To separate the nanocarriers from the oily phase, the resulting oily solution was redispersed in deionized (DI) water or PBS to separate the nanocarriers from the oily phase, followed by centrifugation. The water phase contained nanocarriers, which were collected by filtering through a single-use filter cartridge (cellulose acetate syringe filter, model DISMIC-13, Advantec). Finally, a dialysis step was performed using a dialysis membrane (molecular weight cut off of 1 kDa) to remove any small molecules suspended in the solutions for 24 h.

Physicochemical Characterization and Stability Monitoring. The mean size, distribution, and ζ potential of the nanocarriers were determined using a Zetasizer Nano (Malvern, Westborough, MA). Measurements were taken at a scattering angle of 173° and a constant temperature of 25 °C. The morphology of the nanocarriers was characterized using transmission electron microscopy (TEM; JEM-3010, Japan). The TEM samples were prepared by drying a droplet of the nanocarrier suspension on a 400 mesh-size carbon film-coated copper grid (Ted Pella Inc.). Then, the grid was placed on a drop of 2% (w/v) sodium phosphotungstate solution for negative staining. On the basis of the TEM images, the size distribution data was obtained by counting more than 190 particles. The stability of the nanocarriers was monitored by measuring their size for 6 months at different time intervals, during which period the nanocarrier solution (concentration: 1 mg/mL) was stored at 4 °C in DI water.

Determination of Entrapment Ratio of 5-ALA. The determination of the content of 5-ALA entrapped in the spherical nanocarrier was based on a comparative analytical method using a 2,4,6-trinitrobenzenesulfonic acid kit (Thermo Fisher). The primary amine group in 5-ALA was quantified after the nanocarrier solution (1 mg/mL) was entirely lyophilized. The total amount of 5-ALA in 1 mL of solution was estimated based on the fit of the standard linear curve.

Degradation Test by Hyaluronidase (HAase). To confirm the effect of enzyme degradation, the degradation of nanocarriers by HAase (Sigma) was tested. First, the nanocarrier solution (1 mg/mL) was monitored by measuring the hydrodynamic size for 24 h, after being stored at 4 and 37 °C in DI water and PBS buffers (pH 6.5 and 7.4), respectively). Then, 50 units/mL of HAase was added to each solution, and the stability was repeatedly checked.

Cell Culture. For in vitro assays, six different types of cell lines were used: gastric cancer cell lines, brain cancer cell lines, and fibroblast cell lines. The human gastric adenocarcinoma cell lines MKN-45 and MKN-74, the human glioblastoma U87-MG, the mouse fibroblast cell line 3T3-L1, and the mouse glioma cell line C6 were obtained from the Korean Cell Line Bank (Seoul, Korea). The human fibroblast (HF) was provided by Prof. Hur at Seoul National University Bundang Hospital. MKN-45, MKN-74, and C6 cells were cultured in RPMI 1640 supplemented with 10% fetal bovine serum (FBS) and 1% antibiotics (penicillin−streptomycin). U87-MG and HF were cultured in DMEM supplemented with 10% FBS and 1% antibiotics (penicillin−streptomycin). 3T3-L1 was cultured in DMEM supplemented with 10% bovine calf serum (BCS) and 1% antibiotics (penicillin−streptomycin). All cell lines were incubated in a humidified 5% CO_2 incubator at 37 °C.

Fluorescent Imaging of Cellular Uptake and Receptor Blocking Assay. For fluorescent microscope imaging, all cells were prepared for each condition and the cells at a density of 1×10^4/well were cultured on a 24-well plate at 37 °C in a humidified incubator with 5% CO_2 for 24 h. After washing twice with PBS, the medium was replaced by the serum-free medium containing nanocarriers (at a final concentration of 0.1 mg/mL) with maintenance at 37 °C in a humidified environment with 5% CO_2 for another 1, 3, and 6 h. Subsequently, the cells were washed twice with PBS to remove the nanocarriers. For fixed cell imaging, the cells were treated with 200 mL 4% paraformaldehyde solution for 10 min. The nuclei were stained with 4′,6-diamidino-2-phenylindole (DAPI) (Sigma) for 3 min, and F-actin was stained with phalloidin-AlexaFluor488 (Invitrogen) for 5 min. Finally, the cells were viewed under a fluorescence microscope (Zeiss Z1 AxioObserver). For the CD44 blocking assay, 1 h before the treatment of the nanocarriers, the medium was replaced with serum-free medium containing free hyaluronic acids (HA) polymer (at a final concentration of 10 mg/mL) to block the CD44 receptors after washing twice with PBS; this was followed by the same treatment for the nanocarriers uptake assay over 3 h, as described previously.

Flow Cytometry Analysis. Cells were cultured via the same procedures as those described previously, then the cells at a density of 5×10^4/well were cultured on a 35 mm cell culture dish at 37 °C in a humidified incubator with 5% CO_2 for 24 h. After washing twice with PBS, the medium was replaced with serum-free medium containing nanocarriers (at a final concentration of 0.1 mg/mL) with maintenance at 37 °C in a humidified environment with 5% CO_2 for 3 h. To utilize the receptor blocking experiments as a control group, the same procedure was performed as that described previously but the pretreatment of the free HA polymer was used to block the CD44 receptors. Subsequently, after 3 h, the cells were washed twice with PBS to remove the nanocarriers. The remaining cells were trypsinized and resuspended in 5 mL of PBS solution. After centrifugation, the cells were suspended in 0.5 mL PBS solution, followed by flow cytometry analysis, which was performed on a flow cytometry instrument (BD FACS Aria II flow cytometer, BD Biosciences).

Quantification of PpIX Fluorescence Induced by 5-ALA Nanocarriers. PpIX generation was quantified in each cell line using the adjusted method. Briefly, all prepared cells were cultured onto 24-well plates and incubated in a humidified incubator with 5% CO_2 at 37 °C. After replacing the serum-free media containing nanocarriers (at a final concentration of 0.1 mg/mL), the cells were lyzed with 100 μL of RIPA lysis and extraction buffer (Biosesang) at several time points (0.5, 1, 2, 3, 4, 6, 12, and 24 h) and the extracted solution was transferred into black 96-well plates. After incubating for 4 h, the media was changed to fresh serum-free media to eliminate the effect of nanocarriers. Next, the fluorescence intensity was measured at 410 nm excitation and 635 nm emission using a microplate reader in fluorescence detection mode (Synergy H1, BioTek). To correct for the absolute fluorescence value in cell numbers, the fluorescence intensities were adjusted against proteins extracted from the cells, wherein the protein concentration of each cell line was estimated based on the bicinchoninic acid (BCA) assay (Thermo Fisher)

Cytotoxicity. All cells were cultured on 96-well plates for in vitro cytotoxicity screening in a humidified incubator with 5% CO_2 at 37 °C. The effect of the nanocarriers on cell viability was determined using a cell counting kit 8 (CCK-8) (Dojindo Lab, Tokyo, Japan). Briefly, all cells were seeded in 96-well plates at a density of 5×10^3 cells/well. After preincubation for 24 h, the cells were treated with various concentrations of nanocarriers (0.062, 0.125, 0.25, 0.5, 1, and 2 mg/mL) for 6, 12, and 24 h at 37 °C. Cells cultured in the medium that did not contain nanocarriers served as the negative control group. At the end of the treatment, CCK-8 solution was added to each well and the plates were incubated for 2 h at 37 °C. The optical density of each well at 450 nm was recorded on a microplate reader (Synergy H1, BioTek).

DOI: 10.1021/acs.biomac.8b01690
Biomacromolecules 2019, 20, 1068−1076

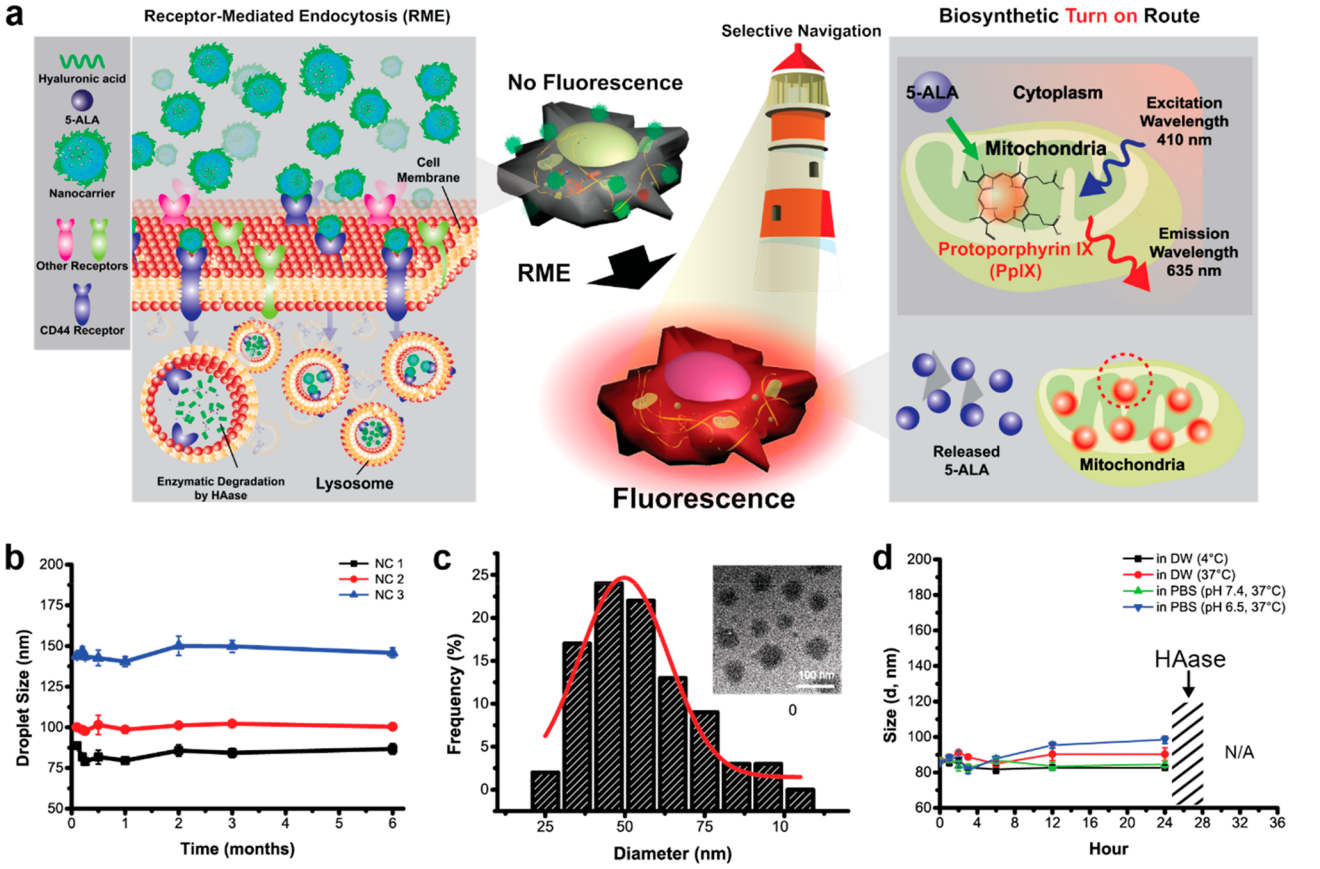

Figure 1. Selective turn-on fluorescence and nanocarrier physicochemical characterization. (a) Schematic illustration showing that cancer cells and nanocarriers have spherical morphologies and are specifically bound to CD44 receptors on cellular membranes, leading to cellular internalization through receptor-mediated endocytosis. In the cytoplasm, internalized nanocarriers encapsulated by lysosomes can be sequentially degraded by the HAase enzyme. Breaking of the polymeric structure of the nanocarriers led to the release of the entrapped 5-ALA into the cytoplasm. In turn, 5-ALA was converted to natural fluorescent materials and protoporphyrin IX (PpIX) through the mitochondrial biosynthetic pathway. (b) Stability profiles for three different types of nanocarriers (NC 1−3), monitored using dynamic light scattering equipment for 6 months under storage conditions of 4 °C and 1 mg/mL in DI water. (c) Particle-size distribution of NC1 from counting over 190 particles and analyzing the TEM images. The inset is a representative TEM image of NC1. Scale bar = 100 nm. (d) Confirmation of the effect of enzymatic degradation through size monitoring using dynamic light scattering equipment. For 24 h, NC1 was stored under different conditions (DI water, PBS, temperature, and pH) and was maintained without any variation in size. After treatment with 50 units/mL of HAase, the size of NC1 started fluctuating and subsequent size data could not be obtained.

Cancer Selective Targeting in Coculture Models. To evaluate the selective uptake in three types of coculture models (C6/MKN-74, 3T3-L1/MKN-74, and HF/MKN-45), all cells were incubated under the same conditions as those described previously. Mixtures of cells with different ratios from 2:1 to 1:10 were seeded onto 24-well plates with different total numbers of cells per well (low, 5×10^4/well; mid, 1×10^5/well; and high, 2×10^5/well). The C6/MKN-74 cell mixture was cultured in RPMI 1640 supplemented with 10% FBS and 1% antibiotics (penicillin−streptomycin). The 3T3-L1/MKN-74 cell mixture was cultured in DMEM supplemented with 10% BCS and 1% antibiotics (penicillin−streptomycin). The HF/MKN-45 cell mixture was cultured in DMEM supplemented with 10% FBS and 1% antibiotics (penicillin−streptomycin). After 12 h of preincubation, these cells were replenished with medium containing nanocarriers (at a final concentration of 0.1 mg/mL) and incubated for 1, 2, 3, and 6 h., After washing twice in PBS, the same processes were performed for fixation, DAPI staining, and F-actin staining, and then each well was sealed using a round cover glass to prevent the wells from drying out. All cells were visualized under a fluorescence microscope, and representative photographs were taken.

Fluorescent Live-Cell Imaging. For live-cell imaging, MKN-74 cells and the cocultured cells (MKN-74/3T3-L1) were prepared for each condition described previously at a total density of 5×10^4/mL on a 35 mm confocal cell imaging dish for 24 h. The nuclei were stained with DAPI for 3 min, and then, after being washed twice with PBS, the serum-free medium containing nanocarriers (at a final concentration of 0.1 mg/mL) was added. Real-time fluorescent live-cell images were obtained using a fluorescence microscope equipped with live-cell incubating chambers at 37 °C with 5% CO_2 for 6 h at 5 min time intervals. The time-lapse images were analyzed and exported to video files using the Zeiss Zen II software program.

Animal Studies. Mouse breeding was conducted in the Laboratory Animal Resources facility at Woojungbsc, Co. Ltd. (Suwon, Korea). The mice were housed in a 12 h day/night cycle and provided with adequate food and water. All animal experiments were in compliance with the guidelines of the Institutional Animal Care and Use Committee. Six- to eight-week-old male athymic Balb/c mice were purchased from Orient Biotech (Seoul, Korea). The athymic nude mice were inoculated with fibrin gel subcutaneously over the right forelimb armpit by injection with MKN-45 cells (1×10^7). To determine the best condition for inoculation before gelation, fibrinogen from bovine plasma (Sigma) containing the cell pellet and thrombin from bovine plasma (Sigma) were mixed at optimal concentrations to the sol/gel transition in 10−15 s. After inoculation (day 3 and day 14), the nanocarriers (1 mg/mL injection of 100 μL volume) were repeatedly injected subcutaneously into the same mice via the same method used to deliver the nanocarriers locally. Additionally, 5-ALA molecules were injected into the same mouse

DOI: 10.1021/acs.biomac.8b01690
Biomacromolecules 2019, 20, 1068−1076

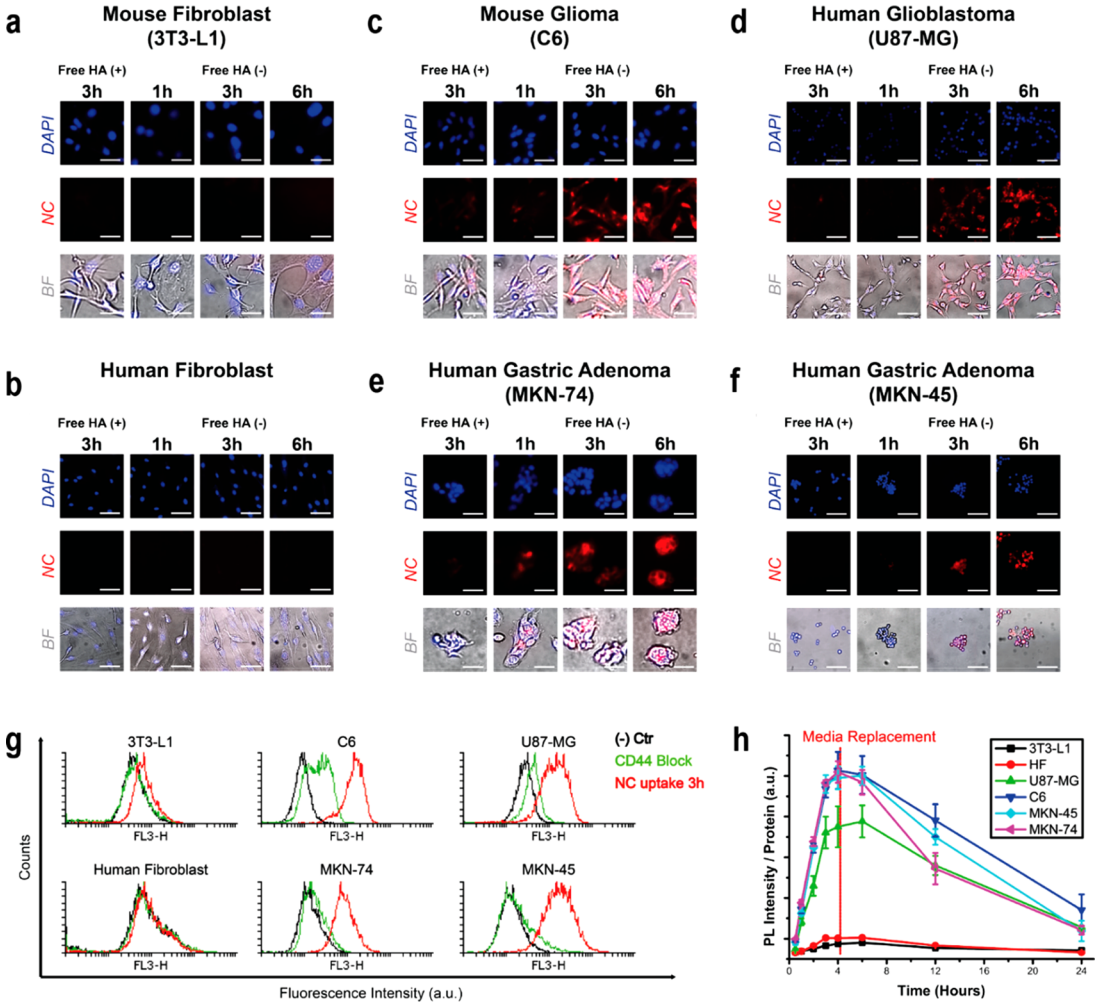

Figure 2. In vitro cellular uptake analysis. (a) Mouse fibroblast (3T3-L1). (b) Human fibroblast (HF). (c) Mouse glioma (C6). (d). Human glioblastoma (U87-MG). (e) Human gastric adenoma (MKN-74). (f) Human gastric adenoma (MKN-45). Intracellular fluorescence signal observation for 1, 3, and 6 h to verify the selective targeting of fluorescence turn-on signals: nucleus (DAPI staining, blue), PpIX (red). Scale bar = 50 μm. The observation process of fluorescence turn-on signals was assessed using a fluorescence microscope with an equivalent nanocarrier concentration of 0.1 mg/mL. The CD44 receptor blocking study was performed through pretreatment with 10 mg/mL of HA for 1 h. No fluorescent signals were observed after 3 h in the blocking groups of all cell lines. (g) The flow cytometric analysis of PpIX generated by nanocarriers in six cell lines after uptake for 3 h: nontreatment is the negative control (black line), uptake by nanocarriers upon pretreatment with 10 mg/mL of HA for 1 h to block CD44 receptors (green line), and uptake by nanocarriers (red line). The uptake concentration was equivalent to 0.1 mg/mL. (h) Quantification of PpIX generated by selective targeting of nanocarriers in six cell lines. The vertical axis was adjusted by the ratio PpIX PL intensity/proteins, where the PL intensity of PpIX was measured in the lyzed cells and the value of proteins in each cell was quantified through the BCA assay. The red vertical line at 4 h indicates the replacement of medium cultured with nanocarriers to fresh medium to verify the effect of nanocarriers on PpIX generation. Each data point indicates the mean ± SEM (Table S2 vs normal cell group (3T3-L1, HF) at each time point by multiple comparison after a repeated-measure two-way ANOVA).

models as the other control groups. The injected concentration of 5-ALA (50 μg/mL) was determined based on the results and was characterized by the entrapment percentages. Fluorescence imaging was performed at 0, 20, 40, 60, 120, 180, and 240 min, and 24 h postinjection using the in vivo imaging system (IVIS Lumina XRMS, PerkinElmer, CLS136340). The fluorescence signals were acquired under conditions of 420/20 nm excitation and 620/40 nm emission filters.

Immunofluorescence Assay. To determine CD44 and CD31 expression levels, the resected tumors were immunostained based on standard immunofluorescence protocols using the following antibodies: anti-CD31 antibody (rat antimouse, BD Pharmingen 553370), Alexa Fluor 594 goat antirat IgG (H+L) antibody (Life Technologies, A-11007), and anti-CD44-FITC antibody (rat antimouse, eBioscience, 11−0441−82). Prior to microscopy, the nuclei were counterstained. The stained slides were visualized under a fluorescence microscope.

Survival Rate and Weight Variation. To monitor the concentration-dependent survival rate and its consequent weight variation, 21 mice were randomly divided into 3 groups (7 in each group) and injected with nanocarriers at different concentrations (1, 3, and 5 mg/mL, respectively). The mice received an intravenous administration of approximately 100 μL of nanocarrier solution. Once a week, 4 injections were administered to each group, and the body weights of the mice in each group was tracked during the survival study. The mice were sacrificed 28 days after the first injection of nanocarriers.

Statistical Analysis. For in vitro experiments (quantification of PpIX fluorescence, Table S2), data were collected as triplicates of individual experiments at each time point (n = 3). Statistical analyses were performed using the GraphPad Prism 7 software program (GraphPad-Prism Software Inc., San Diego, CA). Data were assessed through two-way analysis of variance (ANOVA).

DOI: 10.1021/acs.biomac.8b01690
Biomacromolecules 2019, 20, 1068−1076

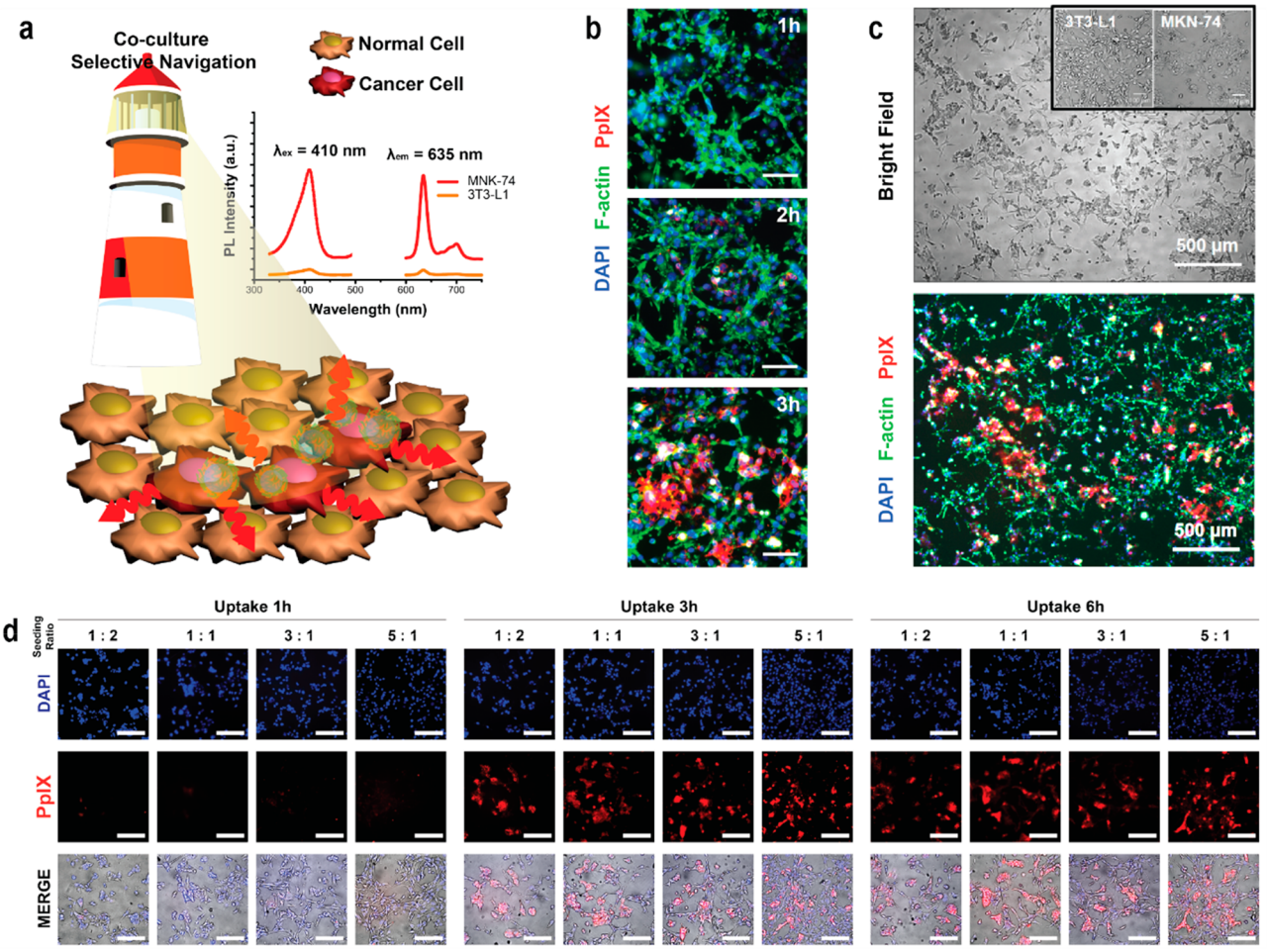

Figure 3. In vitro selectivity in a coculture model. (a) Scheme of selective targeting to cancer cells. The lighthouse represents cancer-illuminating fluorescence signals on specific cells toward 3T3-L1 and MKN-74 cell mixtures. The inset represents the PL intensity obtained from the lyzed cells: MKN-74 (red line) and 3T3-L1 (orange line), where the excitation wavelength was 410 nm and the emission wavelength was 635 nm. (b) Representative merged fluorescence images of selective turn-on fluorescence signals generated by nanocarriers under the coculture condition with a mixture of MKN-74 and 3T3-L1 cells. The fluorescence signals were observed for 1, 2, and 3 h. Scale bar = 100 μm. (c) Bright (upper) and merged fluorescence images at low magnification, showing the selective turn-on PpIX signals in cancer cells. The inset represents the morphologies of two cells (3T3-L1 and MKN-74) at high density displaying phenotypical differences. Scale bar = 500 μm. (d) Fluorescence images showing the ability of selective targeting to MKN-74 cells surrounded by different densities of 3T3-L1 cells. The seeded number of MKN-74 cells was fixed to 1×10^4 cells/well, and the seeded number of 3T3-L1 cells increased. The seeding ratio of 3T3-L1/MKN-74 varied from 1:2 to 5:1. The fluorescence signals were observed for 1, 3, and 6 h. Nucleus (blue), F-actin (green), and PpIX (red).

RESULTS AND DISCUSSION

Nanocarriers were mainly composed of HAs to address the specificity. HAs provide skeletal structures of polymeric nanocarriers and act as anti-CD44 membrane epitopes[26−30] that are overexpressed in most cancer cells. Nonfluorescent 5-ALA,[17,31,32] which is known to be transformed to a fluorescent moiety via the biosynthesis pathway in cells, is physically incorporated in HA nanocarriers. Once delivered to cancer cells by receptor-mediated endocytosis, the nanocarriers turn-on distinctive fluorescent lights as shown in Figure 1a. Cancer cells can be selectively lit up by excitation, thus showing the distinguishable light themselves. We achieved significant enhancement of sensitivity by minimizing the fluorescence background via a selective turn-on strategy.

The nanocarriers were manufactured via two steps: water-in-oil (W/O) emulsification and phase transfer technique (Figure S1a). After the W/O emulsification, a large number of particles were trapped within the oily phase. By transferring the entrapped particles to a water phase, large quantities of homogeneous particles were obtained, which showed excellent stability for more than 6 months without diffusion of the entrapped molecules (Figure 1b). The size of the nanocarriers, measured by TEM, was on average 53.58 nm and displayed a spherical shape (Figure 1c, Figure S1b−e). This result was corroborated by dynamic light scattering (Figure S1f). The characterization results of different nanocarriers (NC1−3; size, zeta potential, 5-ALA entrapment ratio) are summarized in Table S1. All in vitro and in vivo experiments were performed using NC1.

To verify the release of 5-ALA encapsulated inside the structure of the nanocarriers in the cells, we performed an enzymatic degradation test,[33] assuming the effect of HAase (Figure 1d). The nanocarrier that was stably maintained for 24 h under different conditions began to be affected by the HAase within 4 h. This clearly demonstrates the effect of HAase on the nanocarrier. The nanocarrier was electrostatically entangled with anionic HA polymer and 5-ALA via partial interaction through ionic bonding; thus, the cleavage of HA

DOI: 10.1021/acs.biomac.8b01690
Biomacromolecules 2019, 20, 1068−1076

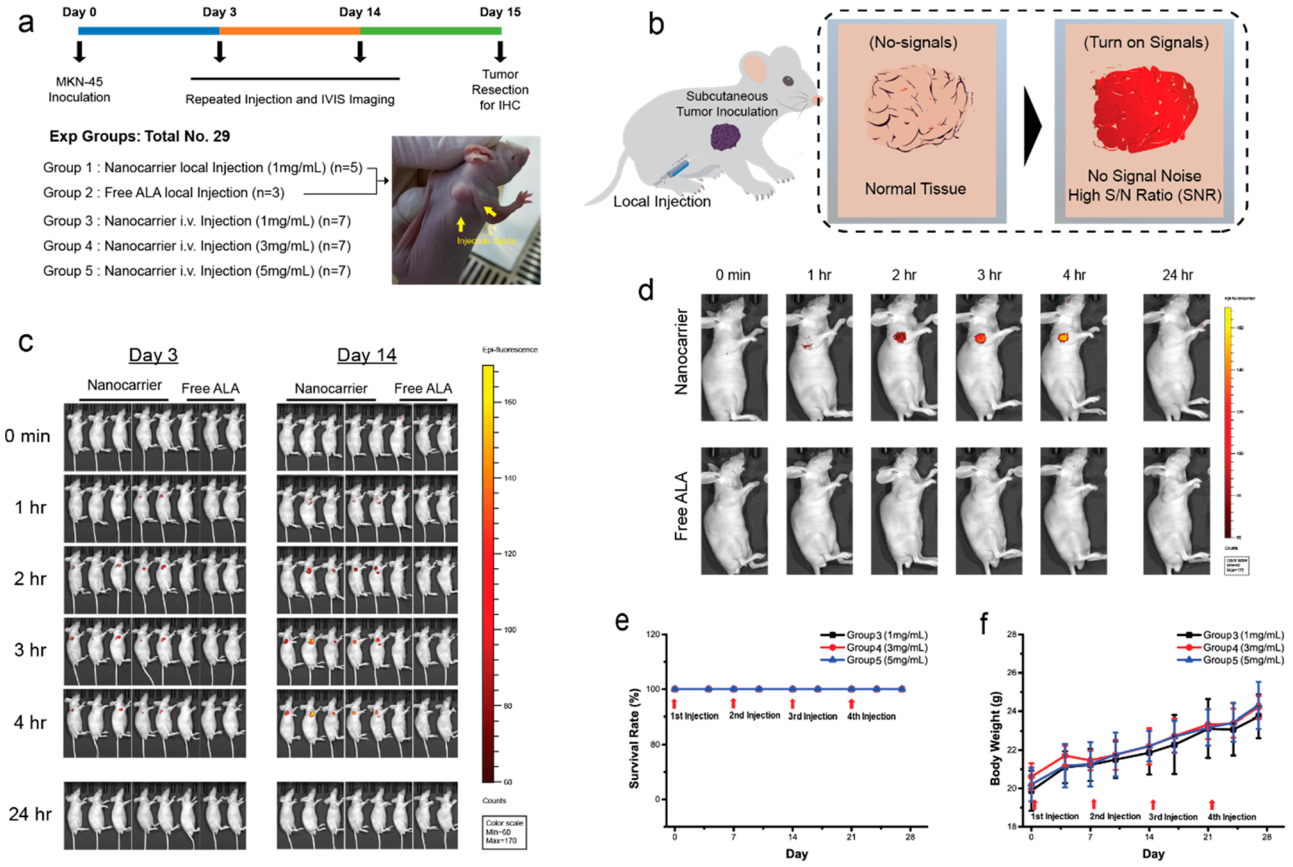

Figure 4. In vivo studies of the efficacy and toxicity of nanocarriers. (a) Description of experimental design of animal studies: in vivo fluorescence imaging performed on two groups and in vivo toxicity test via intravenous injection performed on three groups. The total number of mice used was 29. After MKN-45 tumor inoculation (1×10^7 cells/injection), in vivo imaging system (IVIS) fluorescence imaging was performed repeatedly on day 3 and day 14, and mice were sacrificed 24 h after the complete degradation of nanocarriers from the last injection. Experimental groups for fluorescence imaging were administrated with 1 mg/mL of nanocarriers injected locally around the tumor site, with yellow arrows indicating the administration spots in the photograph of the mouse with tumor inoculated subcutaneously over the right forelimb armpit. Resected tumor specimens were examined from immunohistochemistry on day 15. (b) Scheme of selective turn-on signals on tumor lesions, leading to maximized signals-to-noise ratio around cancerous lesions owing to no signal noise. (c) Multiple time-point in vivo fluorescence imaging via local administration in MKN-45 tumor-bearing mice (nanocarrier administration and free 5-ALA administration as the control group). IVIS fluorescence imaging was performed repeatedly on day 3 and day 14. (d) Representative multiple time-point in vivo fluorescence images on day 14 to compare the difference between the comparison group and control group. (e) The survival rate and (f) body weight variation in healthy mice to evaluate the potential toxicity from nanocarriers. Twenty-one mice were randomly divided into three groups. Once a week, four repeated administrations were given to each group, and the body weight of mice in each group was tracked during the survival study. The concentration of nanocarriers intravenously administrated were escalated up to 1, 3, and 5 times that of the tumor mice model for fluorescence images.

polymer chains resulted in nanosized spherical structures that could be broken down, then the entrapped 5-ALA were released to the cytoplasm. The percentage of 5-ALA entrapped inside nanocarriers varied around 5%−10% (Figure S2). Once the nanocarriers specifically undergo CD44 receptor-mediated endocytosis, enzymatic degradation in lysosomes occurs.[26,33,34] High stability in the aqueous solution and their enzymatic degradation property make nanocarriers ideal for long-term storage and use.

Initially, the nanocarriers did not have any fluorescence signal. However, after internalization to cells via RME, released 5-ALA was converted to PpIX by enzymatic degradation (Figure 1a, Figure S3). This specific mechanism is well-known as the pathway of heme biosynthesis.[17] To determine whether the nanocarriers could be selectively targeted to cancer cells, we examined in vitro uptake assays on six cell lines. After 6 h of incubation with nanocarriers, the normal fibroblast cell lines did not display any fluorescence change in the microscope images (Figure 2a,b). Conversely, we observed fluorescence signals gradually appearing 3 h postuptake in four cancer cells (Figure 2c−f), suggesting the specificity of nanocarriers. Furthermore, if the CD44 receptors of the cells were blocked, fluorescence intensity could not be observed 3 h postuptake even in cancer cells. The cell uptake suggested from the fluorescence microscopy was confirmed by flow cytometry experiments (Figure 2g). The data not only demonstrated that nanocarriers were efficiently delivered to targeted cells mediated via the CD44 receptor but it also suggested that cancer cells were visualized through fluorescent turn-on signals.

To measure the fluorescence intensity quantitatively, the value of the fluorescence intensity, which is proportional to the number of cells, was adjusted. For adjustment, the PL intensity value was corrected based on the quantity of protein in the cell as analyzed by the BCA assay (Figure S4). The adjusted result shown in Figure 2g revealed that the fluorescence signals dramatically increased in cancer cells compared to normal cells. To determine whether the result was affected by nanocarriers, after 4 h, the medium was replaced with serum-free medium

DOI: 10.1021/acs.biomac.8b01690
Biomacromolecules 2019, 20, 1068−1076

without nanocarriers. From this point, the signals gradually decreased because of natural degradation.

The substances constituting the nanocarriers are nontoxic materials, and viability assays (CCK-8) were performed to determine the cytotoxicity of nanocarriers in proportion to the concentration and time (Figure S5). Nanocarriers are mainly composed of two natural components, HA and 5-ALA, which already exist in the body, thus they can be naturally degraded. Even if the cells were introduced at a high concentration, their nontoxic effects were confirmed.

In real tumor microenvironments, cancer cells are surrounded by various cells such as fibroblasts, adipocytes, and endothelial cells with extracellular matrix components.[35,36] We studied in vitro coculture selective targeting models[37] to evaluate whether actual targeting was possible for cancer cells surrounded by normal cells (Figure 3a). Regarding cell morphologies, MKN-74 cells showed a tendency to agglomerate, whereas the spreading pattern of fibroblasts, which showed a typical spindle-shape morphology, was different; thus, we hypothesized that the effect of nanocarriers can be distinguished based on phenotypic traits (Figure S6).

In a cancer/normal cell environment (MKN-74/3T3-L1), we observed that agglomerated cells gradually emitted fluoresence signals (Figure 3b, Video S1). Cells were stained with DAPI and phalloidin-AlexaFluor488 (nuclei (blue) and actin filaments (green), respectively). This showed the targeted efficiency of nanocarriers and selective turn-on fluorescence signals. In addition, in low resolution microscope images, the agglomeration of MKN-74 cells showed distinguishable strong fluorescence signals without background noise (Figure 3c). Regardless of the number of fibroblast cells near MKN-74 cells and the total number of cells seeded on the dish, the same result was obtained (Figure 3d, Figure S7). Cocultured conditions with cancer/normal cells (MKN-45/HF) corroborated this selectivity to cancer cells (Figure S8). In contrast, fluorescence signals appeared on all cells over time in a cancer/cancer cell environment (C6/MKN-74) (Figure S9). Taken together, the results demonstrated that the targeting efficiency of nanocarriers is excellent, even in a coculture environment.

Our goal was to precisely turn-on targeted cancer lesions in vivo. Accordingly, experimental procedures were designed for repeated local injection around the tumor site (Figure 4a). After inoculation of MKN-45 cells, the time interval of injection was set sufficiently to eliminate the effects of nanocarriers on mice. Turn-on signals have the potential to minimize background noise, which results in much higher sensitivity.[4,38] As depicted in Figure 4b, if the fluorescence signal was only turned on in tumor lesions, it would maximize the signal-to-noise ratio. After local injection of the nanocarrier, strong fluorescent signals for tumor inoculated lesions were gradually turned on, as expected (Figure 4c,d). Particularly, we observed that fluorescence intensity was maximized between 3 and 4 h. No fluorescent signals could be observed in nontumor bearing mouse injected via the same method used to deliver nanocarriers (Figure S10). By contrast, all mice in the controls, that had administration of free 5-ALA, showed nondistinctive fluorescence features. From the fluorescence immuno-labeling analysis, CD44 and CD31 expression levels were confined to the resected tumor section (Figure S11).

During the experiment of repeated local injections, all mice survived without any changes in their physical activity. As potential toxicity is fundamentally important, a toxicological test was conducted via intravenous administration of nanocarriers in nontumor bearing healthy mice. Even when administrated at concentrations up to five times that of the IVIS image, all mice were unaffected by the nanocarriers (Figure 4e,f). Nanocarriers proved to have no toxic effect, which was the same result as that found from the in vitro study.

5-ALA is already used in clinical applications.[9] However, its clinical use is highly limited to malignant tumor resection (e.g., glioma and glioblastoma in WHO grade III and IV)[39] and the beneficial effects of 5-ALA have not been clearly confirmed in clinical practice.[40] Little is known regarding its delivery and accumulation mechanism. The most prevalent and widely accepted hypothesis suggests that the enzyme configuration in malignant cells plays a role; however, this is still up for debate.[17,31] Zwitterionic 5-ALA alone does not show selectivity to cancer cells owing to a lack of targeting moiety, and it is not permeable to lipid bilayers.[41] Our study aimed to validate the selective delivery of 5-ALA via nanocarriers using an engineered approach rather than support either of the hypotheses above. Hence, we presented selective internalization to cancer cells and tumor lesions that were substantiated by the data, where the anti-CD44 moiety carried RME internalization and released 5-ALA in the cytoplasm. Regardless of the current controversy on PpIX accumulation in cancer cells, if nanocarriers successfully deliver 5-ALA to cancer cells, this accumulated fluorescence feature would be a great advantage.

The concept of nanoparticles in tandem with 5-ALA has been demonstrated to actively deliver to cancerous lesions. However, the reported strategies have not yet solved the associated problems of efficacy, safety, and mass-production.[12,25] In addition, the cellular effects are not yet fully understood regarding the chemical modification of 5-ALA or ALA derivatives on biological aspects. Metabolic disorders such as porphyria are closely associated with defects in heme biosynthesis.[42] Although the heme biosynthesis route has been well studied, it might not be adequate for the chemical modification used for the enhanced delivery of 5-ALA. Therefore, the best method is to deliver it without modification because 5-ALA and its derivatives are natural materials in the body.

Our results from the coculture targeting models demonstrated remarkable selectivity of the nanocarrier in a coculture environment. Thus, our methods offer a new strategy beyond conventional in vitro testing that efficiently targets specifically single cell lines. However, it would not be negligible with regard to cell-to-cell communication, cytokine, and other biological factors.[36] In addition to the in vitro models, we studied the effect of repeated local injections to demonstrate the efficacy and validity of our nanocarriers in an in vivo mouse model. Among many routes of administration, the intravenous route is commonly used for injections in small rodent models; however, in our study, we observed a decreased efficacy with highly delayed turn-on signals to tumors. Much evidence has suggested that the delivery efficacy of nanoparticles into tumors remains a major challenge for the clinical translation of nanoparticles.[43] Considering many biological factors in the body (e.g., blood circulation, immune response, renal clearance, and so on), more research is still required to validate the animal model that is most adequate and ideal for tumor-targeting studies. There is plenty of scope for future research regarding fluorescence-based precise diagnosis, real-

DOI: 10.1021/acs.biomac.8b01690
Biomacromolecules 2019, 20, 1068−1076

time tumor resection, and cytoreductive treatment with photodynamic therapy.

CONCLUSIONS

The present study described the design of a polymeric nanocarrier encapsulating fluorophore precursors. Our approach to the fabrication of the nanocarrier would be very simple to mass-produce. The nanocarrier is highly stable, allowing for long-term storage and reduction in manufacturing costs. Evidently, the results of both in vitro and in vivo studies demonstrated nontoxicity, targeting efficiency (selectivity), and selective navigation of turn-on signals (sensitivity). Therefore, our strategies are expected to escape the addressed issues in the field and will be extremely fast in the application of the next steps. The results from the present study provide a perspective for next generation imaging agents in cancer diagnosis. Future studies should focus on demonstrating in vivo accurate surgical resections as well as strive to extend cytoreductive treatment with photodynamic therapy to prevent tumor recurrence.

ASSOCIATED CONTENT

Supporting Information

The Supporting Information is available free of charge on the ACS Publications website at DOI: 10.1021/acs.biomac.8b01690.

Scheme of fabrication steps, characterization data, cytotoxicity, morphologies of mixed cell images, and fluorescence images under the coculture condition as well as additional data for animal studies (PDF)

Fluorescence video under coculture condition (AVI)

AUTHOR INFORMATION

Corresponding Authors

*E-mail: kangwonlee@snu.ac.kr. Phone: +82-31-888-9145.
*E-mail: wongun@yonsei.ac.kr. Phone: +82-2-2123-5755.

ORCID

Won-Gun Koh: 0000-0002-5191-2531
Kangwon Lee: 0000-0001-5745-313X

Notes

The authors declare no competing financial interest.

ACKNOWLEDGMENTS

This research was supported by the Bio & Medical Technology Development Program of the National Research Foundation funded by the Ministry of Science, ICT & Future Planning (grant number: No. NRF-2016R1D1A1B03932220, NRF-2017M3A7B4049848, NRF-2017M3D1A1039289). The comments provided by Prof. David J. Mooney (Harvard University, Cambridge, MA, USA) were greatly appreciated and they were invaluable in improving the quality of our manuscript.

REFERENCES

(1) Weissleder, R.; Tung, C. H.; Mahmood, U.; Bogdanov, A., Jr. In vivo imaging of tumors with protease-activated near-infrared fluorescent probes. *Nat. Biotechnol.* **1999**, *17* (4), 375−8.

(2) Terai, T.; Nagano, T. Fluorescent probes for bioimaging applications. *Curr. Opin. Chem. Biol.* **2008**, *12* (5), 515−21.

(3) Olson, E. S.; Jiang, T.; Aguilera, T. A.; Nguyen, Q. T.; Ellies, L. G.; Scadeng, M.; Tsien, R. Y. Activatable cell penetrating peptides linked to nanoparticles as dual probes for in vivo fluorescence and MR imaging of proteases. *Proc. Natl. Acad. Sci. U. S. A.* **2010**, *107* (9), 4311−4316.

(4) Weaver, J. B. Bioimaging: Hot nanoparticles light up cancer. *Nat. Nanotechnol.* **2010**, *5* (9), 630−1.

(5) Kotov, N. Bioimaging: The only way is up. *Nat. Mater.* **2011**, *10* (12), 903−4.

(6) Yao, J.; Yang, M.; Duan, Y. Chemistry, biology, and medicine of fluorescent nanomaterials and related systems: new insights into biosensing, bioimaging, genomics, diagnostics, and therapy. *Chem. Rev.* **2014**, *114* (12), 6130−78.

(7) Doane, T. L.; Burda, C. The unique role of nanoparticles in nanomedicine: imaging, drug delivery and therapy. *Chem. Soc. Rev.* **2012**, *41* (7), 2885−911.

(8) Choi, H. S.; Gibbs, S. L.; Lee, J. H.; Kim, S. H.; Ashitate, Y.; Liu, F.; Hyun, H.; Park, G.; Xie, Y.; Bae, S.; Henary, M.; Frangioni, J. V. Targeted zwitterionic near-infrared fluorophores for improved optical imaging. *Nat. Biotechnol.* **2013**, *31* (2), 148−53.

(9) Vahrmeijer, A. L.; Hutteman, M.; van der Vorst, J. R.; van de Velde, C. J. H.; Frangioni, J. V. Image-guided cancer surgery using near-infrared fluorescence. *Nat. Rev. Clin. Oncol.* **2013**, *10* (9), 507−518.

(10) Schnermann, M. J. Chemical biology: Organic dyes for deep bioimaging. *Nature* **2017**, *551* (7679), 176−177.

(11) Zhang, R. R.; Schroeder, A. B.; Grudzinski, J. J.; Rosenthal, E. L.; Warram, J. M.; Pinchuk, A. N.; Eliceiri, K. W.; Kuo, J. S.; Weichert, J. P. Beyond the margins: real-time detection of cancer using targeted fluorophores. *Nat. Rev. Clin. Oncol.* **2017**, *14* (6), 347−364.

(12) Bobo, D.; Robinson, K. J.; Islam, J.; Thurecht, K. J.; Corrie, S. R. Nanoparticle-Based Medicines: A Review of FDA-Approved Materials and Clinical Trials to Date. *Pharm. Res.* **2016**, *33* (10), 2373−87.

(13) Eifler, A. C.; Thaxton, C. S. Nanoparticle therapeutics: FDA approval, clinical trials, regulatory pathways, and case study. *Methods Mol. Biol.* **2011**, *726*, 325−38.

(14) Anselmo, A. C.; Mitragotri, S. Nanoparticles in the clinic. *Bioengineering & translational medicine* **2016**, *1* (1), 10−29.

(15) Van Dam, G. M.; Themelis, G.; Crane, L. M.; Harlaar, N. J.; Pleijhuis, R. G.; Kelder, W.; Sarantopoulos, A.; De Jong, J. S.; Arts, H. J.; van der Zee, A. G. Intraoperative tumor-specific fluorescence imaging in ovarian cancer by folate receptor-α targeting: first in-human results. *Nat. Med.* **2011**, *17* (10), 1315.

(16) Uchiyama, K.; Ueno, M.; Ozawa, S.; Kiriyama, S.; Shigekawa, Y.; Yamaue, H. Combined use of contrast-enhanced intraoperative ultrasonography and a fluorescence navigation system for identifying hepatic metastases. *World J. Surg.* **2010**, *34* (12), 2953−2959.

(17) Ismail, M. S.; Dressler, C.; Obele, S. S.; Daskalaki, A.; Philipp, C.; Berlien, H. P.; Weitzel, H.; Liebsch, M.; Spielmann, H. Modulation of 5-ALA-induced PpIX xenofluorescence intensities of a murine tumour and non-tumour tissue cultivated on the chorio-allantoic membrane. *Lasers in medical science* **1997**, *12* (3), 218−25.

(18) Shi, L.; Wang, X.; Zhao, F.; Luan, H.; Tu, Q.; Huang, Z.; Wang, H.; Wang, H. In vitro evaluation of 5-aminolevulinic acid (ALA) loaded PLGA nanoparticles. *Int. J. Nanomed.* **2013**, *8*, 2669−76.

(19) Chung, C. W.; Chung, K. D.; Jeong, Y. I.; Kang, D. H. 5-aminolevulinic acid-incorporated nanoparticles of methoxy poly-(ethylene glycol)-chitosan copolymer for photodynamic therapy. *Int. J. Nanomed.* **2013**, *8*, 809−19.

(20) Xu, H.; Liu, C.; Mei, J. S.; Yao, C. P.; Wang, S. J.; Wang, J.; Li, Z.; Zhang, Z. X. Effects of light irradiation upon photodynamic therapy based on 5-aminolevulinic acid-gold nanoparticle conjugates in K562 cells via singlet oxygen generation. *Int. J. Nanomed.* **2012**, *7*, 5029−5038.

(21) Tong, H.; Wang, Y.; Li, H.; Jin, Q.; Ji, J. Dual pH-responsive 5-aminolevulinic acid pseudopolyrotaxane prodrug micelles for enhanced photodynamic therapy. *Chem. Commun.* **2016**, *52* (20), 3966−9.

(22) Wu, J.; Lin, Y.; Li, H.; Jin, Q.; Ji, J. Zwitterionic stealth peptide-capped 5-aminolevulinic acid prodrug nanoparticles for targeted photodynamic therapy. *J. Colloid Interface Sci.* **2017**, *485*, 251−259.

DOI: 10.1021/acs.biomac.8b01690
Biomacromolecules 2019, 20, 1068−1076

(23) Han, H.; Jin, Q.; Wang, H.; Teng, W.; Wu, J.; Tong, H.; Chen, T.; Ji, J. Intracellular Dual Fluorescent Lightup Bioprobes for Image-Guided Photodynamic Cancer Therapy. *Small* **2016**, *12* (28), 3870−8.
(24) Wu, J.; Han, H.; Jin, Q.; Li, Z.; Li, H.; Ji, J. Design and Proof of Programmed 5-Aminolevulinic Acid Prodrug Nanocarriers for Targeted Photodynamic Cancer Therapy. *ACS Appl. Mater. Interfaces* **2017**, *9* (17), 14596−14605.
(25) Babič, A.; Herceg, V.; Ateb, I.; Allémann, E.; Lange, N. Tunable phosphatase-sensitive stable prodrugs of 5-aminolevulinic acid for tumor fluorescence photodetection. *J. Controlled Release* **2016**, *235*, 155−164.
(26) Toole, B. P. Hyaluronan: from extracellular glue to pericellular cue. *Nat. Rev. Cancer* **2004**, *4* (7), 528−39.
(27) Ahrens, T.; Sleeman, J. P.; Schempp, C. M.; Howells, N.; Hofmann, M.; Ponta, H.; Herrlich, P.; Simon, J. C. Soluble CD44 inhibits melanoma tumor growth by blocking cell surface CD44 binding to hyaluronic acid. *Oncogene* **2001**, *20* (26), 3399.
(28) Dufay Wojcicki, A.; Hillaireau, H.; Nascimento, T. L.; Arpicco, S.; Taverna, M.; Ribes, S.; Bourge, M.; Nicolas, V.; Bochot, A.; Vauthier, C.; Tsapis, N.; Fattal, E. Hyaluronic acid-bearing lipoplexes: physico-chemical characterization and in vitro targeting of the CD44 receptor. *J. Controlled Release* **2012**, *162* (3), 545−52.
(29) Lee, Y.; Lee, H.; Kim, Y. B.; Kim, J.; Hyeon, T.; Park, H.; Messersmith, P. B.; Park, T. G. Bioinspired surface immobilization of hyaluronic acid on monodisperse magnetite nanocrystals for targeted cancer imaging. *Adv. Mater.* **2008**, *20* (21), 4154−4157.
(30) Rios de la Rosa, J. M.; Tirella, A.; Gennari, A.; Stratford, I. J.; Tirelli, N. The CD44 Mediated Uptake of Hyaluronic Acid Based Carriers in Macrophages. *Adv. Healthcare Mater.* **2017**, *6* (4), 1601012.
(31) Eickhoff, A.; Jakobs, R.; Weickert, U.; Hartmann, D.; Schilling, D.; Alsenbesy, M.; Eickhoff, J. C.; Riemann, J. F. Long-Segment early squamous cell carcinoma of the proximal esophagus: curative treatment and long-term follow-up after 5-aminolevulinic acid (5-ALA)-photodynamic therapy. *Endoscopy* **2006**, *38* (6), 641−3.
(32) Kaneko, S.; Kaneko, S. Fluorescence-Guided Resection of Malignant Glioma with 5-ALA. *Int. J. Biomed. Imaging* **2016**, *2016*, 6135293.
(33) Wang, J.; Liu, J.; Liu, Y.; Wang, L.; Cao, M.; Ji, Y.; Wu, X.; Xu, Y.; Bai, B.; Miao, Q. Gd Hybridized Plasmonic Au Nanocomposites Enhanced Tumor Interior Drug Permeability in Multimodal Imaging Guided Therapy. *Adv. Mater.* **2016**, *28* (40), 8950−8958.
(34) Jiang, T.; Mo, R.; Bellotti, A.; Zhou, J.; Gu, Z. Gel−liposome mediated co delivery of anticancer membrane associated proteins and small molecule drugs for enhanced therapeutic efficacy. *Adv. Funct. Mater.* **2014**, *24* (16), 2295−2304.
(35) Kessenbrock, K.; Plaks, V.; Werb, Z. Matrix metalloproteinases: regulators of the tumor microenvironment. *Cell* **2010**, *141* (1), 52−67.
(36) Shiga, K.; Hara, M.; Nagasaki, T.; Sato, T.; Takahashi, H.; Takeyama, H. Cancer-Associated Fibroblasts: Their Characteristics and Their Roles in Tumor Growth. *Cancers* **2015**, *7* (4), 2443−2458.
(37) Le Droumaguet, B.; Nicolas, J.; Brambilla, D.; Mura, S.; Maksimenko, A.; De Kimpe, L.; Salvati, E.; Zona, C.; Airoldi, C.; Canovi, M. Versatile and efficient targeting using a single nanoparticulate platform: application to cancer and Alzheimer's disease. *ACS Nano* **2012**, *6* (7), 5866−5879.
(38) Chan, J.; Dodani, S. C.; Chang, C. J. Reaction-based small-molecule fluorescent probes for chemoselective bioimaging. *Nat. Chem.* **2012**, *4* (12), 973−84.
(39) Louis, D. N.; Perry, A.; Reifenberger, G.; von Deimling, A.; Figarella-Branger, D.; Cavenee, W. K.; Ohgaki, H.; Wiestler, O. D.; Kleihues, P.; Ellison, D. W. The 2016 World Health Organization Classification of Tumors of the Central Nervous System: a summary. *Acta Neuropathol.* **2016**, *131* (6), 803−20.
(40) Stummer, W.; Pichlmeier, U.; Meinel, T.; Wiestler, O. D.; Zanella, F.; Reulen, H. J.; Group, A. L.-G. S. Fluorescence-guided surgery with 5-aminolevulinic acid for resection of malignant glioma: a randomised controlled multicentre phase III trial. *Lancet Oncol.* **2006**, *7* (5), 392−401.
(41) Walter, S.; Susanne, S.; Simon, W.; Herbert, S.; Clemens, F.; Claudia, G.; Alwin, E. G.; Rainer, K.; Hans, J. R. Intraoperative detection of malignant gliomas by 5-aminolevulinic acid-induced porphyrin fluorescence. *Neurosurgery* **1998**, *42* (3), 518−526.
(42) Layer, G.; Reichelt, J.; Jahn, D.; Heinz, D. W. Structure and function of enzymes in heme biosynthesis. *Protein Sci.* **2010**, *19* (6), 1137−61.
(43) Jiang, W.; von Roemeling, C. A.; Chen, Y. X.; Qie, Y. Q.; Liu, X. J.; Chen, J. Z.; Kim, B. Y. S. Designing nanomedicine for immuno-oncology. *Nat. Biomed Eng.* **2017**, *1* (2), 0029.

DOI: 10.1021/acs.biomac.8b01690
Biomacromolecules 2019, 20, 1068−1076